JTTEE5 16:831–838
DOI: 10.1007/s11666-007-9074-z
1059-9630/$19.00 © ASM International

Electromagnetic and Mechanical Properties of Silica-Aluminosilicates Plasma Sprayed Composite Coatings

F. Cipri, C. Bartuli, T. Valente, and F. Casadei

(Submitted February 27, 2007; in revised form July 3, 2007)

The physico-chemical and thermo-mechanical properties of aluminosilicate ceramics (high-melting point, low thermal expansion coefficient, excellent thermal shock resistance, low-density and good corrosion resistance) make this class of materials a good option for high-temperature structural applications. Al_2O_3-SiO_2 compounds show an excellent refractory behavior allowing a wide use as wear-resistant thermal barrier coatings, in metallurgical and glass plants and in high temperature heat exchangers. Moreover, the low values of thermal expansion coefficient and of complex permittivity allow to extend the use of this ceramic for microelectronic devices, radome for antennas and electromagnetic windows for microwaves and infrared. The present article presents the results of an extensive experimental activity carried out to produce thick aluminosilicate coatings by plasma-spray technique. The APS deposition parameters were optimized on the basis of a surface response approach, as specified by design of experiments (DoE) methodologies. Samples were tested for phase composition, total porosity, microstructure, microhardness, deposition efficiency, fracture toughness, and modulus of rupture. Finally, coatings were characterized for their particularly interesting electromagnetic properties: complex permittivity was measured at microwave frequency using a network analyzer with wave guide.

Keywords air plasma spray, alumina-silica, permittivity, complex permeability

1. Introduction

Meta-silicates materials, the main components of the MgO-Al_2O_3-SiO_2 system, are widely applied in the coating and refractory industries. Among the most interesting features of these ceramic materials are very low coefficient of thermal expansion (CTE), good thermal and chemical stability, high mechanical strength and thermal shock resistance and low-complex permittivity (Ref 1).

More specifically, aluminosilicate ceramics, such as $3Al_2O_3{\cdot}2SiO_2$, present an orthorhombic crystal lattice without any polymorphic transitions up to 1580 °C; this thermodynamical stability prevents any volume change and allows excellent thermal shock resistance and high strength at temperatures as high as 1500 °C (Ref 2). Moreover, the presence of silica reduces oxygen permeability of such materials with respect to pure alumina, making them suitable as protective coatings for high temperature applications such as for heat exchangers, gas turbines and internal combustion engines (Ref 3, 4).

Finally, aluminosilicates feature very low loss factors, being therefore, widely used in electrical and electronic engineering applications as high voltage insulating materials, devices for microelectronics, electromagnetic windows, sensor field and high frequency applications (Ref 5, 6).

Silica-based thermal-spray coatings are rarely reported in scientific papers and their chemical, mechanical, thermal, and above all, electronic properties are not exhaustively presented in the current literature (Ref 7, 8).

The present article presents the results of an experimental activity aimed to produce thick plasma-sprayed aluminosilicate coatings matching the good mechanical properties and optimal spraying aptitude of alumina with the excellent corrosion resistance and dielectric properties of silica.

2. Materials and Methods

Agglomerated powders of 40wt.% Al_2O_3-60wt.% SiO_2 were produced from commercial raw materials (Metco 105SFP alumina and Fluka 83340 quartz); in order to achieve the desired flowability and optimize deposition efficiency, starting powders were milled together in a

This article is an invited paper selected from presentations at the 2007 International Thermal Spray Conference and has been expanded from the original presentation. It is simultaneously published in *Global Coating Solutions, Proceedings of the 2007 International Thermal Spray Conference*, Beijing, China, May 14-16, 2007, Basil R. Marple, Margaret M. Hyland, Yuk-Chiu Lau, Chang-Jiu Li, Rogerio S. Lima, and Ghislain Montavon, Ed., ASM International, Materials Park, OH, 2007.

F. Cipri, C. Bartuli, and **T. Valente**, Department of Chemical & Materials Engineering, Sapienza University of Rome, Rome, Italy; and **F. Casadei**, Centro Sviluppo Materiali, Rome, Italy. Contact e-mail: bartuli@uniroma1.it.

planetary milling (Retsch PM100): the stainless steel jar was loaded with 2/3 alumina/silica ratio in weight plus 20 alumina balls (diameter 12.7 mm) and the rotation speed was set at 500 rpm for 12 h. Finally, the powders were agglomered by spray-drying processing (NIRO Atomizer Mobile Minor™).

Size distribution of the composite particles was analyzed by laser-light scattering (Malvern Mastersizer) in a liquid dispersant (ethylic alcohol). A round shape of all particles was assumed for the final calculation of the particle size from the scattering angle of the laser beam.

Silica-aluminosilicates composite coatings were deposited onto stainless steel substrates using a controlled atmosphere plasma spray system (CAPS, produced by Sulzer Metco) operating in a close pressure-vessel in APS configuration.

Plasma-spray operating parameters were selected using statistical design of experiments by implementing a two-factors second order and three levels surface response factorial plan. Hydrogen gas flow rate and torch-substrate spraying distance were also selected as the two variable process parameters likely to affect the total thermal and kinetic energy transferred from the plasma plume to the powders and the dwell time for physical and chemical transformations affecting the deposit composition (Ref 9, 10).

Standard operating parameters for the deposition of alumina coatings were selected as central point of the experimental matrix; H_2 flow rate was varied in the range of [12÷18] slpm and spray distance was varied in the range of [80÷140] mm (respectively 20 and 27% of variation compared to central point). The complete matrix for the 13 experimental runs is reported in Table 1.

Highlighted test conditions identify the central point of the matrix, whose conditions were reproduced for five test runs in order to calculate the statistical variance of the process and the measurement systems; to avoid experimental traps the tests order was randomized. Other standard deposition parameters kept constant for all test runs are reported in Table 2.

Three goal functions were selected among the most representative properties of coatings: microhardness, coating porosity and deposition rate.

Table 1 Experimental matrix for the two-factors, three levels, second order factorial plan

Test run	Sample	Spray distance, mm	H_2 flow rate, slpm
9	1	140	18
1	2	80	12
8	3	140	15
5	**4**	**110**	**15**
12	**5**	**110**	**15**
10	**6**	**110**	**15**
13	**7**	**110**	**15**
11	**8**	**110**	**15**
6	9	110	18
2	10	80	15
4	11	110	12
3	12	80	18
7	13	140	12

Table 2 Spray parameters constant for all test runs

Torch type	Metco F4MB
Pressure and gas	1 bar-Air
Torch-substrate velocity (mm/s)	500
Pressure and cooling gas	8 bar-Ar
Ar plasma gas flow rate (slpm)	45
H_2 plasma gas flow rate (slpm)	12-15-18
Plasma current (A)	550
Plasma voltage (V)	73
Powder carrier gas (slpm)	3 Ar

Metallographic samples from each coating were prepared by polishing (400, 600, 800, and 1200 silicon-carbide grit plates) and lapping (9, 6, 3 and 1 micron diamond suspension pastes on naps), and thickness and porosity of the coatings were evaluated by optical microscopy (Nikon Eclipse L150) with the aid of image analysis software systems (Leica Qwin V. 2.2 and Lucia™ 4.80).

Phase composition was investigated by X-ray diffraction (Siemens D500, Cu kα radiation, 0.01° step size—1 s per step).

Microhardness was evaluated by means of a LEICA VMHT Vickers indenter (5 g normal load applied for 15 s) as an average of 35 measurements.

Tribological and thermomechanical performance of brittle coatings are strictly correlated with the fracture toughness, K_c, assessing the capability of material to resist to the propagation of microcracks (Ref 11, 12).

Fracture toughness, K_c, was calculated according to the Evans and Wilshaw model (Ref 12) by measuring the length of microcracks (parallel to the coating) generated at the tips of the imprint by the indenter; 35 measurements with 25 g normal load applied for 15 s were carried out to obtain a statistical population of data. A possible effect of artificial improvement of K_c induced by the presence of porosities in the coating must be taken into the due account when comparing the values of toughness measured on anisotropic lamellar coatings by indentation techniques with those obtained for dense isotropic ceramic bodies.

Every data population was treated by statistical elaboration software (Statistica 6.0, Stat-Soft Inc.), in order to identify and remove measures that do not respect the normal distribution. Outliers values, evidenced by plotting data population in a normal plot, were removed (4 at most) before any statistical operation.

Modulus of rupture (MoR) and Young's modulus of the coatings were evaluated by a four-point bending tests (Zwick/Roell testing machine; Spider 8 strain gage acquisition unit), in order to minimize the effect of defects (microcracks, porosity, inclusions) on the results of test (Ref 13); in fact four-point bending, compared to three points, allow to distribute the maximum stress on a larger surface, thus producing statistically more consistent results. The theory of the composite beam was applied to extrapolate the values of the modulus from stress-strain curves, with the two basic hypotheses of perfect substrate-coating adhesion and homogeneous-coating thickness. The continuity of strains and displacements caused by

flexural strength are the basis of the composite beam theory, valid even when the sample is composed by two different materials. The elastic modulus of the coating E_c (GPa) was evaluated by the following equation:

$$E_C = \frac{\frac{M}{K} E_S I_S}{I_C}$$

where M (Nm) is the momentum applied during the test, E_S is the Young modulus of the substrate, I_C and I_S (m^4) are the moment of inertia of coating and substrate, respectively, and the beam curvature K (m^{-1}) is calculated as:

$$K = \varepsilon / y$$

where ε is the longitudinal strain and y is the distance between the coating surface and neutral surface inside the beam.

Stainless steel beams, 100×10×5 mm, were used as substrates. The thickness of the deposit was 850 μm. in order to guarantee uniform testing conditions, all tested samples were ground to the final size. For a more precise measurement of strain signals, two strain gages per sample were pasted with epoxy glue in the middle of both sides (surfaces of deposit and back of substrate). Sampling time was fixed at 10 Hz.

Finally, electromagnetic properties (Ref 14) of aluminosilicate coatings were measured by means of a network analyzer (VNA HP 8720-D) with wave-guide technique (WR90, X-band 8-12 GHz). Complex permittivity and permeability represent the dielectric and magnetic characteristics of every material; to know these four values (two real and two imaginary) a system of four equation has to be solved from the values of reflection and transmission coefficients (S11 and S12) measured inside the wave guide.

This technique is widely used for measuring complex characteristic of polymers, and only very rarely for ceramics, because of the difficulties encountered in the precision machining of the samples. In the case of coatings, the presence of a metallic substrate does not allow us to use the common transmission geometry, so that, a new set of equations had to be purposely developed to evaluate the complex permittivity by mean one single reflection test. Alluminosilicates do not show magnetic properties, thus it is reasonable to assume complex permeability equal to 1 and use coefficient S11 to evaluate the complex permittivity.

The sample to be inserted inside the special holder is a block whose dimensions (22.86×10.16×6.00 mm) are strictly determined, with only a few microns of tolerance; to machine self standing coatings more than 6 mm thick is extremely complicated and expensive, due to the very high number of coatings cracked and spoiled during either spraying or machining. Thus, two composite blocks were cut from a stainless steel plate coated with a 3.5 mm thick deposit; every side of each sample was ground and lapped in order to obtain the dimensions within the requested tolerances.

3. Results and Discussion

3.1 Design of Experiments

Figure 1 shows the size distribution of agglomered aluminosilicate powders. The average diameter is about 38 μm and the distribution guarantees optimal flowability.

In the bright field light/optical micrograph of a cross section of a single-agglomerated granule (Fig. 2), the two different ceramic phases (quartz and α alumina) can be identified.

Typical aluminosilicate plasma coatings are shown in Fig. 3(a) and (b).

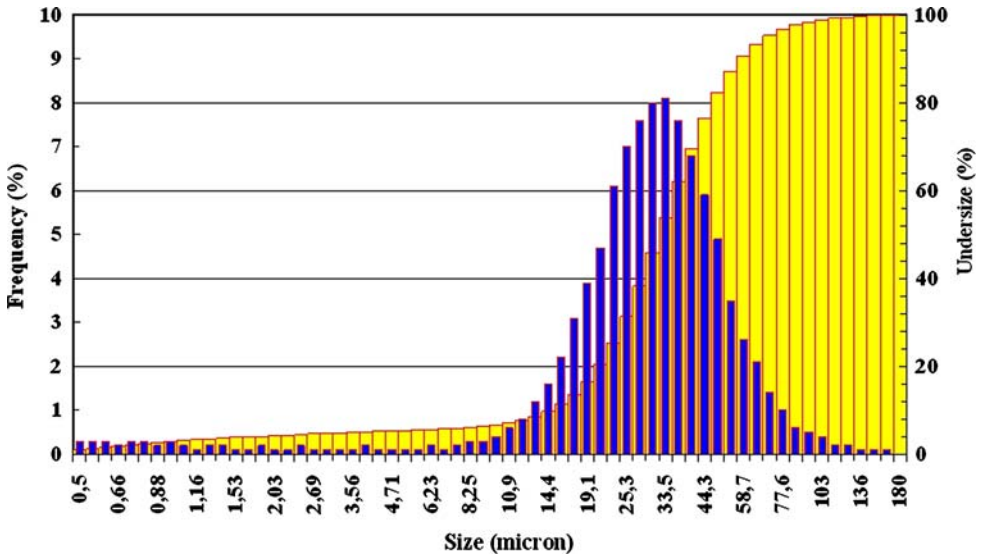

Fig. 1 Size distribution (frequency histogram and cumulative curve) of spray-dried alumina-silica agglomerated powders; average diameter D[4,3] = 38 μm

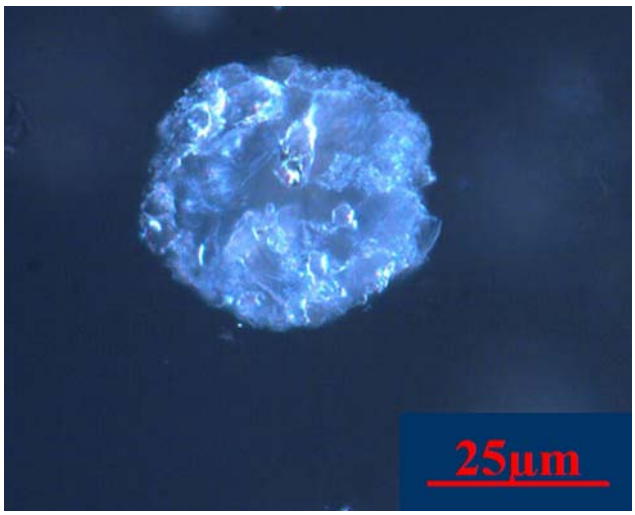

Fig. 2 Optical micrograph (BF, 500×) of a spray dried alumina-silica composite powder granule

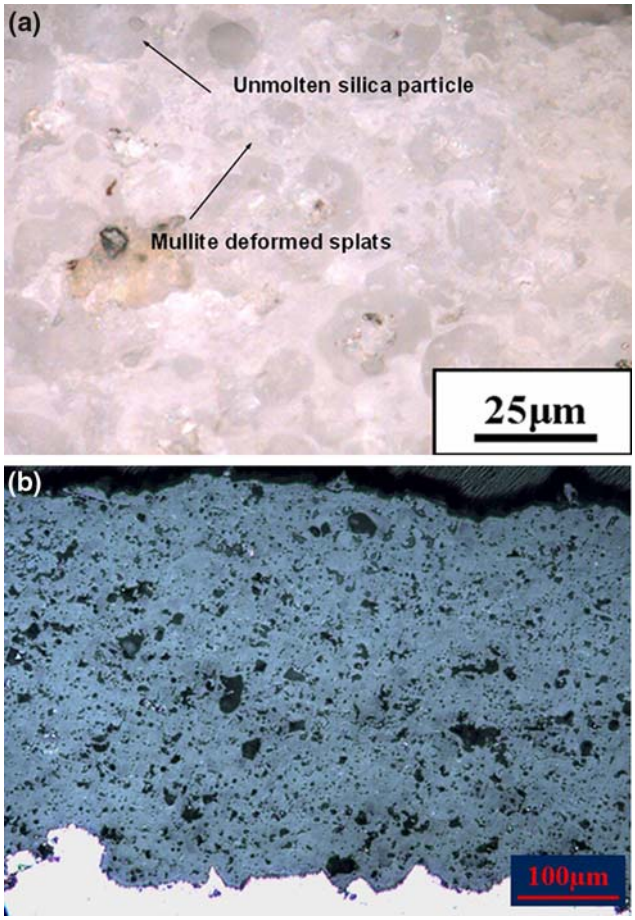

Fig. 3 Optical micrographs of aluminosilicates coating: (a) BF 1000×; (b) BF 100×

It is a common experience in thermal-spray practice that the pure silica powders cannot be efficiently sprayed and deposited: in fact the temperature window between the melting point of the oxide and the temperature at which silica is reduced to gaseous phases is narrow. Moreover, thermal conductivity of the material is low (1.3-1.4 W/mK, depending on the degree of crystallinity), so that in the very short times necessary to heat the powders and project them to the substrate, only an outer shell of limited thickness of the particle can effectively be molten, and the solid particles bounce off the substrate on impact.

In the case of alumina-silica agglomerated particles, on the other hand, part of the silica reacts with alumina to form low-melting compounds, principally mullite, that allow to produce composite deposits characterized by the typical lamellar microstructure, in which rounded unmolten silica particles (dark gray in Fig. 3a) are kept together by low melting mullite deformed splats (lighter in Fig. 3a).

All samples show good adhesion to the substrate; no defect or detachment was evidenced at the substrate-coating interface (see Fig. 3b).

Selected process parameters have a strong influence on the microstructure of the deposits; longer dwell times and higher plasma energies allow for in-flight reactions between alumina and silica to form low-melting compounds. On the other hand, low H_2 flow rates and shorter dwell times in the plasma plume cannot guarantee the complete solution of silica in molten alumina, and the microstructure is characterized by the presence of several unmolten particles mainly composed of silica (Fig. 3a).

In Fig. 4, XRD patterns from two representative samples may be compared. Pattern a is relative to coating n. 2 (produced with a short spray distance of 80 mm and a low hydrogen flow rate of 12 slpm) and clearly evidences the presence of high amounts of SiO_2 and some unmarked peak imputable to substochiometric oxides. The presence of metastable phases in the coatings is consistent with the adopted process parameters, which minimize the dwell time of powders and the enthalpy of the plasma, therefore, producing unmolten and unreacted silica particles in a substoichiometric alumino-silicate matrix.

On the contrary, spray conditions of sample n.1 (140 mm; 18 slpm) allow long-enough time and high-enough enthalpy to achieve a more complete solution of silica in alumina, producing coatings mainly consisting of $Al_6Si_2O_{13}$ (that represents the expected phase in accord with the thermodynamic alumina-silica phase diagram), with high residual amounts of silica.

However it is not always easy to identify univocal and unambiguous relationships among spraying parameters and microstructural features, as the analysis is possibly complicated by the role of further complex phenomena, such as the transfer of thermal energy from the high enthalpy plasma to the particles. For this reason the use of a factorial plan is mandatory, in order to maximize performance in a system where factors are not linearly independent.

The complete correspondence among selected variable factors and measured goal functions (with corresponding standard deviations) for all experimental test runs is reported in Table 3. Results of microhardness, porosity

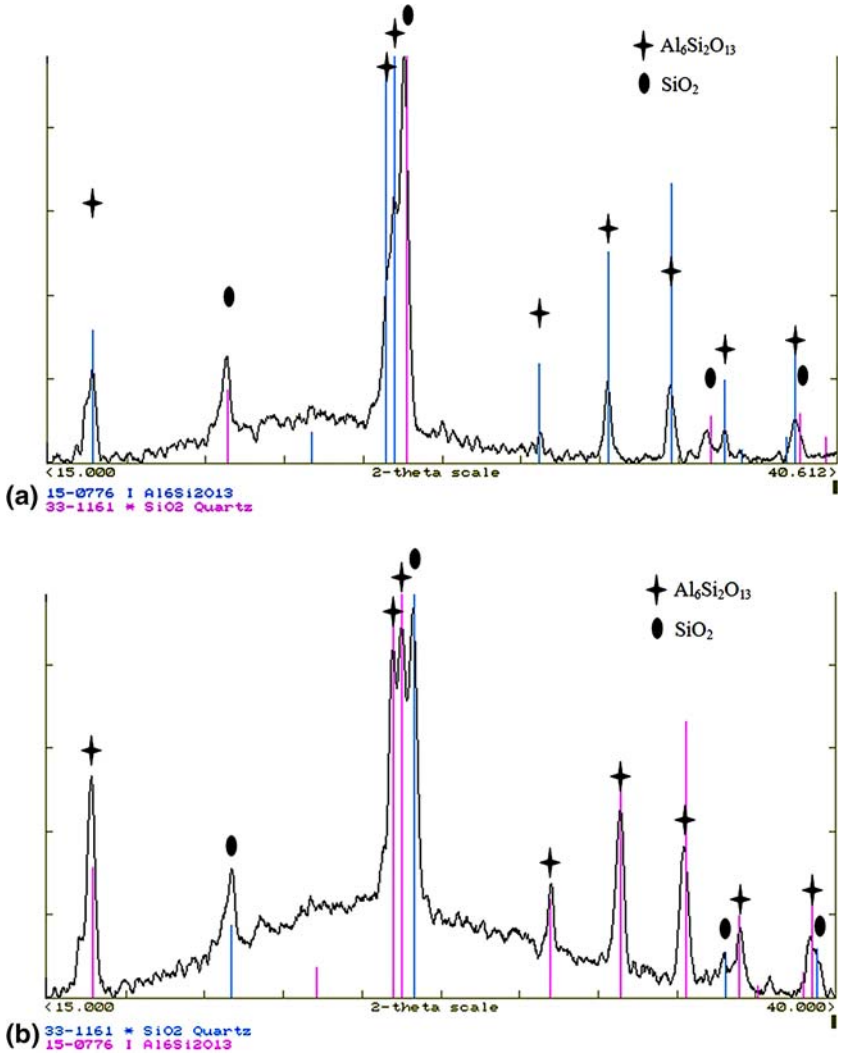

Fig. 4 XRD patterns of samples n.2 (80 mm-12 slpm, a) and n.1 (140 mm-18 slpm, b)

Table 3 Selected factors and measured goal functions for all experimental test runs

Sample	Factor 1	Factor 2	Goal function 1 (Std dev)		Goal function 2 (Std dev)		Goal function 3 (Std dev)	
1	18	140	857.8	(137.8)	10.33	(2.15)	6.45	(0.13)
2	12	80	924.7	(143.7)	7.01	(1.32)	8.32	(0.26)
3	15	140	883.3	(115.6)	11.60	(1.80)	8.02	(0.21)
4	15	110	833.6	(132.8)	8.19	(1.53)	8.29	(0.35)
5	15	110	856.9	(137.1)	7.91	(1.44)	8.68	(0.15)
6	15	110	853.1	(118.8)	10.31	(1.41)	8.19	(0.11)
7	15	110	830.3	(138.5)	7.91	(1.99)	9.14	(0.19)
8	15	110	829.9	(127.9)	8.41	(1.44)	9.16	(0.27)
9	18	110	893.7	(176.2)	9.09	(1.63)	6.70	(0.23)
10	15	80	910.3	(104.5)	8.17	(1.37)	9.02	(0.28)
11	12	110	828.1	(186.1)	9.54	(1.56)	7.31	(0.12)
12	18	80	890.4	(128.6)	7.01	(1.57)	7.28	(0.21)
13	12	140	773.8	(117.1)	8.24	(1.80)	7.58	(0.16)

Factor 1 = H_2 flow rate (slpm)
Factor 2 = Spay distance (mm)
Goal function 1 = Hardness (VHN)
Goal function 2 = Porosity (%)
Goal function 3 = Deposition rate (μm/pass)

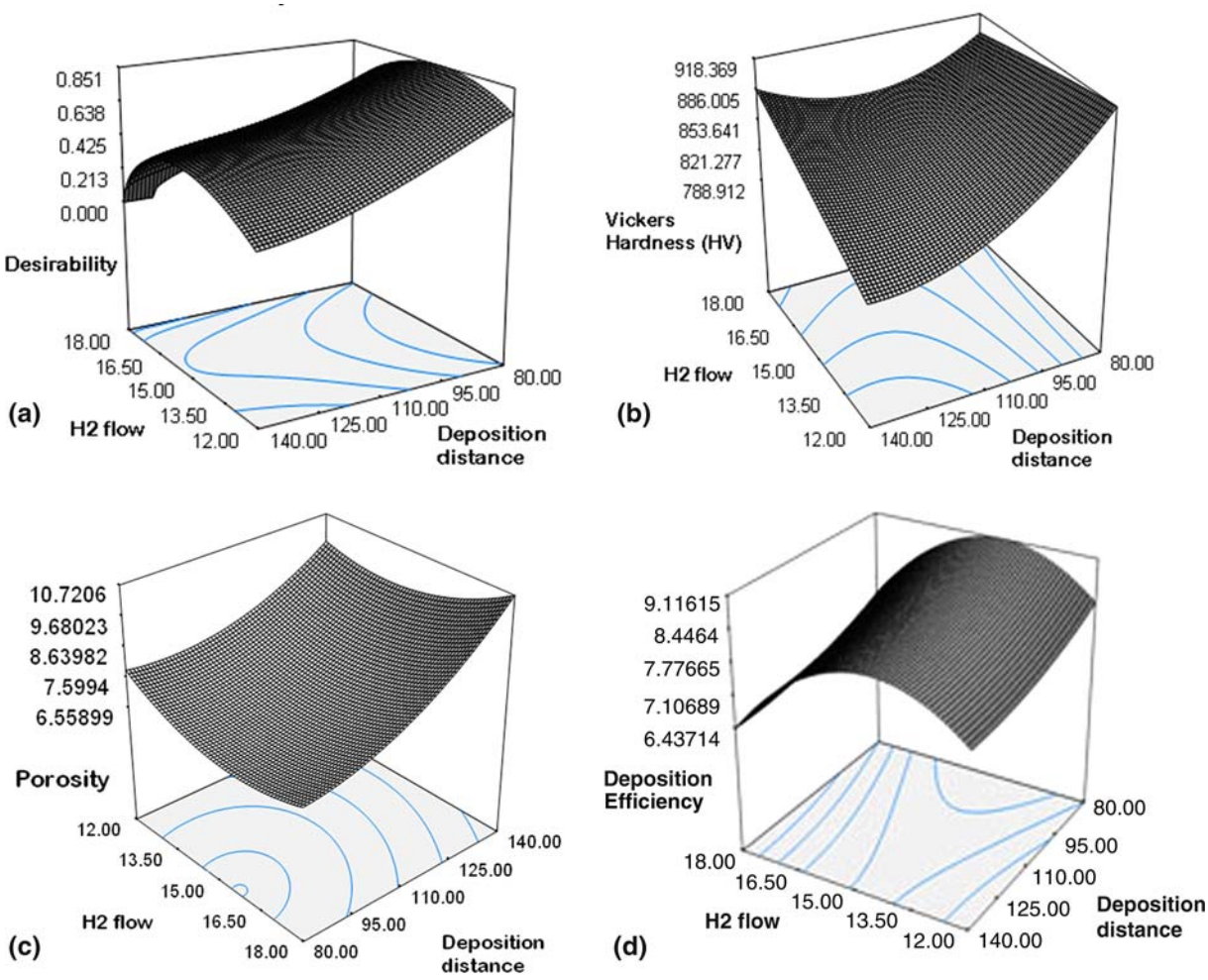

Fig. 5 Response surfaces of DoE: (a) desiderability; (b) microhardness; (c) porosity; (d) deposition rate

Table 4 Optimized factors and expected goal functions

Desirability	H_2 flow, slpm	Spray dist., mm	HV	Porosity, %	Dep. rate, µm/pass.
0.86	14.6	80	910	6.7	9.1

and deposition rate can be related to the spray parameters by observing the responses surfaces obtained by statistical analysis and reported in Fig. 5(a), (b), (c), and (d).

In a factorial plan each goal function may be optimized independently; however, in most cases optimized factors for a goal function could not maximize yet another function. This situation suggests assigning different desirability indices to each goal function and the final target of the DoE will be the optimization of the overall desirability of system. In this case high desirability goal functions are microhardness and porosity, whereas less importance was assigned to deposition rate.

Table 4 summarizes the optimized parameters and the expected responses from the model.

3.2 Optimized Coatings

Bright field micrographs of cross sections of optimized coatings are shown in Fig. 6(a) and (b) where it is possible to recognize the typical lamellar structure of plasma coatings and the presence of unmolten SiO_2 particles.

X-ray diffraction analysis confirmed the presence of silica next to the main $Al_6Si_2O_{13}$ phase.

Microhardness, porosity and deposition rate were measured and average results are reported in Table 5, together with corresponding values of fracture toughness; the measured values are in very good agreement with the values estimated from the statistical model. Estimation of K_c of bulk isotropic materials of similar composition, produced by hot isostatic pressing and sintering (Ref 15, 16) are also in very good agreement with the present results (Ref 16).

Four-point bending tests were carried out to evaluate MoR and elasticity modulus. The distance among supports is fixed at 80 mm for the upper support and 40 mm for the lower one; the sample is tested with coating in tension and substrate in compression. Results are summarized in Table 6.

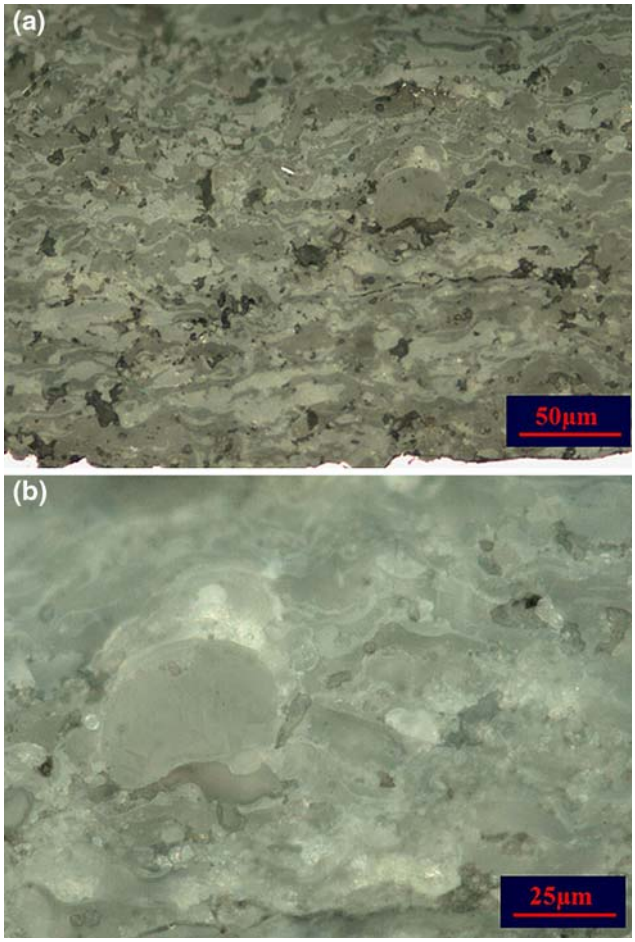

Fig. 6 Optical micrographs of optimized coatings cross sections: (a) BF 200×; (b) BF 1000×

Table 5 Vickers microhardness, porosity, deposition rate and fracture toughness of optimized sample; average measured values are in good agreement with estimated values

	HV	Porosity, %	Dep. rate, µm/pass.	K_c, MPa $m^{1/2}$
Average	897.7	6.40	10.08	2.40
Std. dev.	166.8	0.86	0.30	1.03
Estimated value	910.0	6.70	9.10	1.03
Error (%)	1.3	4.5	9.7	1.03

As shown in Fig. 7 for one of the coatings, at the end of the test each substrate presented a visible plastic deformation; despite the bend no macrocracks or detachment was evidenced, due to excellent properties of adhesion between coating and substrate.

Finally, complex permittivity of the coatings was measured and results are reported in Fig. 8. Figure 9 shows the metal backed samples used for WR-90 X-band measurements.

Aluminosilicates are not polar dielectrics and applied electrical field produces elastic deformations of electronic

Fig. 7 Coated beams after bending test

Table 6 Results of four bending test: young modulus, tensile strain and modulus of rupture

	Young's modulus, GPa	Tensile strain, µm/m	MoR, MPa
Average	43.2	3029	120.8
Std. dev.	16.0	63	41.9

shells (electronic polarization) and ions strains (ionic polarization). Complex permittivity depends on electric field frequency and dipoles capability to follow the field. In the case of high frequencies, dipoles cannot reorient themselves; as a consequence the polar momentum of material decreases and electrical energy is partially dissipated in thermal energy.

In the complex expression of permittivity the real part represents the energy stored, whereas the imaginary part takes into account the dissipation in the dielectric. The plots shown in Fig. 9 evidence values in the range of 7.8 ÷ 6.2 for real permittivity and 0.28 ÷ 0.04 for imaginary part, in good agreement with previous works (Ref 3). However, the frequencies applied for the mentioned investigations were lower than 1 MHz, instead of 10 GHz, and the tests were carried out by impedance techniques.

4. Conclusions

Thick (up to about 3.50 mm) silica-aluminosilicates composite ceramic coatings were produced by air-plasma spray. Coatings exhibited very interesting performance in terms of mechanical properties and, fracture toughness (elastic modulus of 43 GPa and K_c of about 2 MPa $m^{1/2}$ for 850 µm thick coatings) and compliance, efficiently coupling to metallic substrates even after plastic deformation.

The electro-magnetic behavior of the composite deposits was investigated. The common experimental

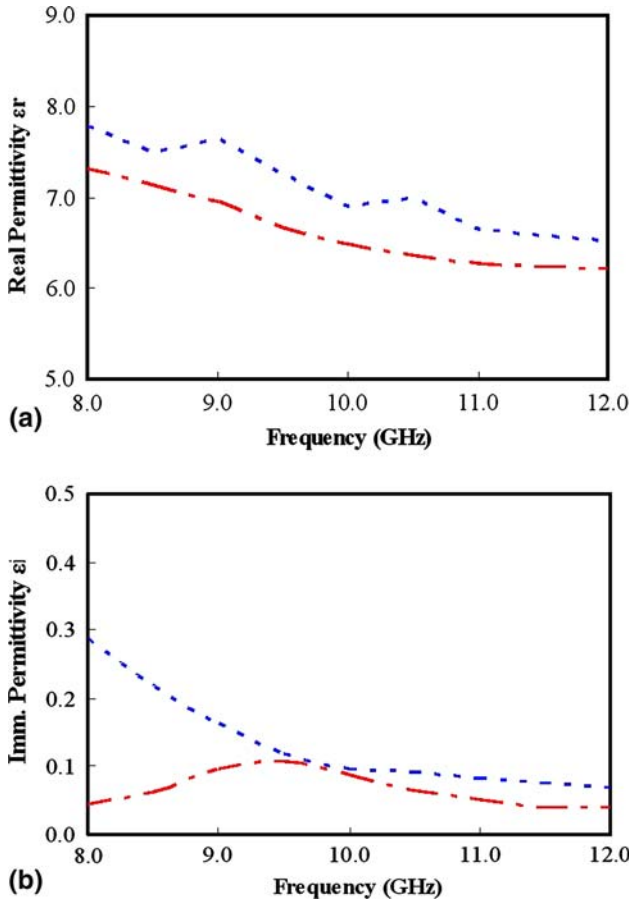

Fig. 8 Plots of complex permittivity of sample 1 (blue dotted line) and sample 2 (red dashed line): (a) real part and (b) imaginary part

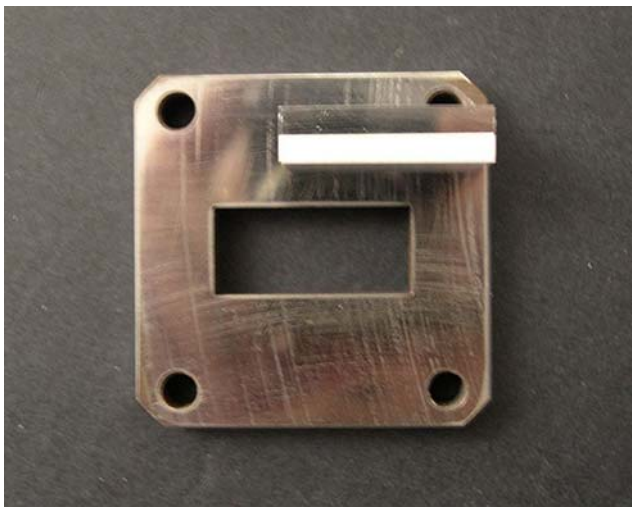

Fig. 9 Metal backed samples for WR-90 X-band holder. Sample size = 22.86 × 10.16 × 6.00 mm; coating thickness = $3^{\pm 0.1}$ mm; substrate thickness = $3^{\pm 0.1}$ mm

procedure for testing of permittivity and complex permeability in X band was adapted for the investigation of metal backed materials with reflection geometry. The measurement of dielectric properties at frequencies of 8-12 GHz can be presented as an original result of particular interest.

Acknowledgments

Dr F. Nanni (University Tor Vergata, Rome) and Dr A. Dell'Aglio (University Roma Tre, Rome) are gratefully acknowledged for electromagnetic measurements and samples testing, respectively.

References

1. S.M. Logvinkov, G.D. Semchenko, D.A. Kobyzeva, V.S. Tolstoi, K.P. Vernigora, and E.S. Sarusa, The Effect of Periodic Reactions in the MgO-Al_2O_3-SiO_2 System on the Phase Composition and Properties of Cordierite-Based Materials, *Refract. Ind. Ceram.*, 2001, **42**(5), p 236-241
2. H. Schneider and E. Eberhard, Thermal Expansion of Mullite, *J. Am. Ceram. Soc.*, 1990, **73**(7), p 2073-2076
3. P. Hou, S.N. Basu, and V.K. Sarin, Structure and High-Temperature Stability of Compositionally Graded CVD Mullite Coatings, *Int. J. Refract. Met. Hard Mater.*, 2001, **19**, p 467-477
4. P.S. Di Mascio, R.M. Orenstein, and H. Rajiyadh, Reliability of a Conceptual Ceramics Gas Turbine Component Subjected to Static and Transient Thermomechanical Loading, *J. Eng. Gas Turb. Power*, 1998, **120**(2), p 263-270
5. P. Ctibor, J. Sedlàček, K. Neufuss, J. Dubský, and P. Chràska, Dielectric Properties of Plasma-Sprayed Silicates, *Ceram. Int.*, 2005, **31**(2), p 315-321
6. A.A. El-Kheshen and M.F. Zawrah, Sinterability, Microstructure and Properties of Glass/Ceramic Composites, *Ceram. Int.*, 2003, **29**(3), p 251-257
7. D. Zhu, N.P. Bansal, K.N. Lee, and R.A. Miller, Thermal Conductivity of Ceramic Thermal Barrier and Environmental Barrier Coating Materials, Technical Memorandum NASA TM-2001-211122, 2001, http://www.gltrs.grc.nasa.gov/citations/all/tm-2001-211122.html
8. P. Rohana, K. Neufuss, J. Matejícek, J. Dubskýa, L. Prchlík, and C. Holzgartner, Thermal and Mechanical Properties of Cordierite, Mullite and Steatite Produced by Plasma Spraying, *Ceram. Int.*, 2004, **30**(4), p 597-603
9. Design-Experiment 5.0.9, Reference Manual (Stat-Ease Inc.), 1989
10. E.P. Box, G. Hunter, and J.S. Hunter, Statistics for Experimenters. John Wiley & Sons, Chichester, NY, 1978
11. B.R. Lawn and E.R. Fuller, Equilibrium Penny-Like Cracks in Indentation Fracture, *J. Mater. Sci.*, 1975, **10**, p 2016-2024
12. A.G. Evans and T.R. Wilshaw, Quasi-Static Solid Particle Damage in Brittle Solids (I) Observations, Analysis and Implications, *Acta Metall.*, 1976, **24**(10), p 939-956
13. J.M. Gere and S.P. Timoshenko, Mechanics of Materials, 4th edn., PWS Pub. Co., Boston (MA), USA, 1997
14. E.F. Knott, J.F. Shaeffer, and M.T. Tuley, Radar Cross Section. SciTech Publishing Inc, Raleigh, NC, 2004
15. R. Torrecillas, G. Fantozzi, S. de Aza, and J.S. Moya, Thermomechanical Behaviour of Mullite, *Acta Mater.*, 1997, **45**(3), p 897-906
16. C. Baudin, Fracture Mechanisms in a Stoichiometric $3Al_2O_32$-SiO_2 Mullite, *J. Mater. Sci.*, 1997, **32**(8), p 2077-2086